



HHS Public Access

Author manuscript

IEEE Sens J. Author manuscript; available in PMC 2024 May 23.

Published in final edited form as:

IEEE Sens J. 2023 November ; 23(21): 25911–25918. doi:10.1109/jsen.2023.3317678.

Optimizing an Optical Cavity-Based Biosensor for Enhanced Sensitivity

Marzhan Sypabekova,

Aidan Hagemann,

Jenna Kleiss,

Cooper Morlan,

Seunghyun Kim [Member, IEEE]

Department of Electrical and Computer Engineering, Baylor University, Waco, TX 76798 USA

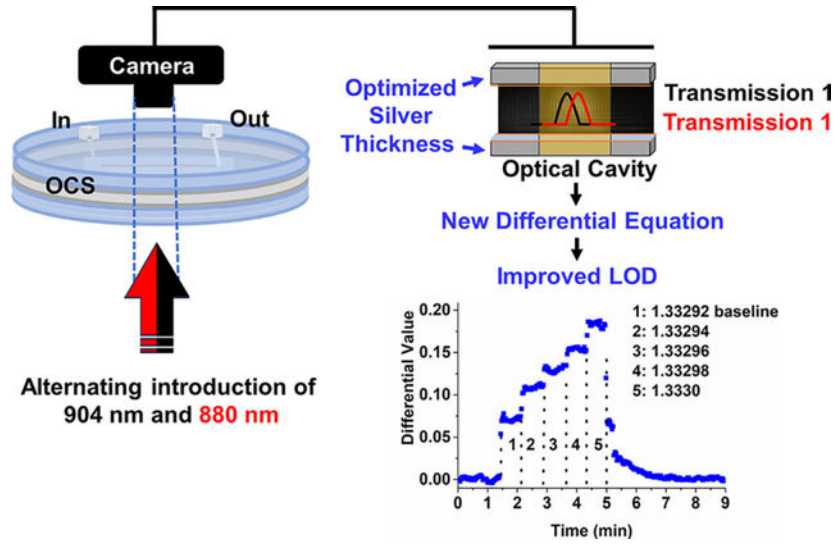
Abstract

The rapid advancement of biosensor technology has revolutionized healthcare, offering improved sensitivity, specificity, and portability. We have developed an optical cavity-based biosensor (OCB) as a promising solution due to its label-free detection, high sensitivity, real-time monitoring, multiplexing capability, and versatility. The OCB consists of an optical cavity structure (OCS), optical components, and a low-cost camera. The OCS is created by two partially reflective surfaces separated by a small gap, where the interaction between target analytes and immobilized receptors leads to a shift in the resonance transmission spectrum, caused by minute changes in the local refractive index (RI). In our previous work, we successfully detected these small changes with a simple OCS and cost-effective components using a differential detection method. Building upon these achievements, this study focuses on optimizing the OCS, improving the camera settings, and enhancing the differential detection approach. By increasing the reflectance of the surfaces and optimizing the optical cavity widths correspondingly, we achieved an improved limit of detection (LOD). We also investigated how the charge-coupled device (CCD) camera shutter time affects the LOD. Additionally, we introduced a new differential equation to further enhance the sensitivity of our system. Through these advancements, we could improve the LOD of the OCB by 7.2 times, specifically for an OCS with a cavity thickness of 9.881 μm and a silver thickness of 46.87 nm. These findings not only contribute to the ongoing effort of optimizing the OCB, but also pave the way for the development of advanced point-of-care biosensors with enhanced detection capabilities.

Graphical Abstract

This work is licensed under a Creative Commons Attribution-NonCommercial-NoDerivatives 4.0 License. For more information, see <https://creativecommons.org/licenses/by-nc-nd/4.0/>

Corresponding author: Seunghyun Kim. (Seunghyun_Kim@baylor.edu).



Keywords

High sensitivity; low limit of detection (LOD); low-cost optical biosensors; optical cavity-based biosensor (OCB); point-of-care biosensors; refractive index (RI) detection

I. INTRODUCTION

BIOSENSORS, combining biological components with physicochemical transducers, have emerged as powerful analytical devices for detecting and analyzing biologically relevant molecules. Biosensor development has witnessed remarkable progress in recent years, with continuous efforts focused on enhancing their sensitivity, selectivity, and usability. Current research in this field is primarily concentrated on three key areas: wearable biosensors [1], point-of-care testing (POCT) biosensors [2], and nanomaterial-based biosensors [3]. Wearable biosensors aim to develop compact, portable devices capable of noninvasive and continuous monitoring of physiological parameters such as glucose levels, heart rate, and biomarkers in sweat and saliva. POCT biosensors focus on decentralized diagnostic testing outside traditional laboratories, providing fast results for diseases like HIV, malaria, COVID-19, and biomarker analysis. Nanomaterial-based biosensors explore nanoparticles, nanowires, and nanotubes for their unique properties, aiming to improve sensitivity and performance in detecting heavy metals, toxins, and biomolecules.

The World Health Organization suggests that POCT biosensors adhere to the ASSURED standard, ensuring affordability, sensitivity, specificity, user-friendliness, rapidness, equipment-free operation, and deliverability to end-users [4], [5]. Currently, centralized diagnostic methods necessitate sending samples to processing laboratories, resulting in prolonged waiting times for results [6], [7], [8]. The widely recognized gold standard diagnostic technology, enzyme-linked immunosorbent assay (ELISA), offers high accuracy [6], [7], [9], [10] but requires complex and time-consuming processes such as labeling [9], [11], [12]. Label-free technologies like surface plasmon resonance (SPR) and total internal reflection ellipsometry (TIRE) provide immediate results and high sensitivity [13], [14] but

suffer from drawbacks such as high cost, space requirements, and the need for specially trained operators [15], [16]. These limitations associated with cost and expertise impede frequent monitoring and can lead to delayed diagnoses [9], [17].

We have developed an optical cavity-based biosensor (OCB) as a promising POCT platform [18], [19], [20], [21], [22], [23], [24]. OCB leverages the optical resonance of an optical cavity structure (OCS), designed to confine and enhance the interaction of light with biological or chemical analytes. The OCS comprises two partially reflective surfaces separated by a small gap. When light propagates through the OCS and travels back and forth, it undergoes multiple beam interference resulting in a resonant characteristic. Due to the highly sensitive nature of optical resonance, the resonance curve shifts with slight changes in the local or bulk refractive index (RI) within the OCS, making the OCB an attractive tool for label-free and highly sensitive detection and real-time monitoring. We developed the OCB with only low-cost components to ensure its affordability. To maximize the sensitivity of this low-cost OCB, we employed a differential detection method [20]. For the differential detection method, the OCS is designed so that the intensity changes of two laser diodes at different wavelengths upon the local or bulk RI change within the OCS are in opposite directions. Then, a differential equation is used to calculate differential values, resulting in a larger change than what is observed with one wavelength. The differential detection method not only improves sensitivity but also offers other benefits for biosensing, such as power equalization (removing dependence on initial power variation for measurement results), a larger dynamic range (detectable concentration range of biomolecules), and larger fabrication tolerance [22]. Our initial biodetection results with the OCB showcased a limit of detection (LOD) of 77.8 ng/mL (1.47 nM) for streptavidin and 43.3 ng/mL (377 pM) for C-reactive protein (CRP) [19].

In this article, we report an improved LOD of the OCB by: 1) optimizing silver thickness; 2) using a longer camera shutter time; and 3) an improved differential equation. The thicker silver layer increases the reflectance of the partially reflective layer of the OCS, increasing the quality (Q) factor and improving the LOD. However, due to the increased absorption of thicker silver layers, there is an optimal silver thickness to achieve the best LOD. A longer camera shutter time helps to increase the overall intensity scale to improve the LOD. The differential equation used for detection also affects the LOD. We demonstrated that an improved differential equation can lower the LOD further by effectively using the intensity ratio changes of both wavelengths. We used bulk RI measurements to demonstrate the improved LODs. The OCS design, fabrication process, test setup, and results are discussed in detail.

II. MATERIALS AND METHODS

A. Materials

Soda lime glass (100 and 76.2 mm) substrates were obtained from UniversityWafer Inc., South Boston, MA, USA, and AZ photoresist (1518) and developer (300 MIF) were obtained from Integrated Micro Materials, Argyle, TX, USA. Spin-on-glass (IC1–200, SOG) was purchased from Futurrex Inc., Franklin, NJ, USA, and SU8 photoresist (SU8–2010) and SU8 developer were purchased from Kayaku Advanced Materials, Inc., Westborough,

MA, USA, UV glue (NOA 86H) was purchased from Norland Products Inc., Jamesburg, NJ, silver etchant (type TFS) was purchased from Transense Company Inc., Danvers, MA, USA 2-propanol (IPA) and acetone (99%) were purchased from Thermo Fisher, Waltham, MA, USA and bovine serum albumin (BSA) and dimethyl sulfoxide (DMSO) were purchased from Sigma, St. Louis, MO, USA.

Laser diodes (A pin code, Ø5.6 mm, 10 mW) at wavelengths 880 and 904 nm, 50:50 nonpolarizing beam splitter (BS) cube (BS014), antireflection (AR)-coated neutral density filter (NF) (NE550B-B), 1" broadband dielectric mirror (BB1-E03), and corresponding mounts for each component (KM100T, CM1-4ER, FMP05, H45) were obtained from Thorlabs Inc., Newton, MA, USA. A charge-coupled device (CCD) camera (CM3-U3-13S2M-CS) was obtained from Point Grey Research Inc., Wilsonville, OR, USA and vacuum pump (MPA2002T1) was obtained from Maxclever Elec Company, Shenzhen, China. All aqueous solutions and rinsing steps were done using deionized (DI) water.

B. Simulation

We used the FIMMWAVE/FIMMPROP (Photon Design, Oxford, U.K.) software for all the simulations performed for the results presented in this article. For more accurate simulations, we first measured the actual center wavelength of the laser diodes with a spectrometer. To investigate the response for different silver thicknesses using simulations, we used 22.5-, 46.9-, 58.3-, and 76.2-nm silver thicknesses measured from samples produced by 15, 22.5, 30, and 37.5 s of sputter deposition time, respectively. An optimal optical cavity width for each silver thickness was determined based on the transmission efficiency for a range of 9.83–10.6 μm . Then, the responses for bulk RI changes with those four different silver thicknesses were calculated and compared.

C. Sample Fabrication

The fabrication process of the OCS is simple and without complex processes. Two low-cost soda lime glass substrates with a thickness of 1 mm and a diameter of 76.2 mm were used to create the channel's top (drilled substrate) and bottom (plain substrate) parts. The fabrication process is illustrated in Fig. 1(a). The inlet and outlet ports of the microfluidic channel on the drilled substrate were created with a 1.6-mm diamond drill (UKAM Industrial Superhard Tool, RPM 9000), Valencia, CA, USA on a benchtop drill press (WEN Products, WEN 4208T), Elgin, IL, USA. Both plain and drilled substrates were cleaned with dust-free swab sticks under DI water to remove any particles from the surface and were then dried under an N_2 stream. A silver layer was sputter-deposited (CRC, Torr LLC), Marlboro, MA, USA on the drilled and plain glass substrates at 60 sccm of Ar and 100-W dc for 15, 22.5, 30, and 37.5 s to create different silver thicknesses. The resulting silver thickness at each time was measured using the profilometer (KLA Tencor, D-500). These silver layers acted as partially reflective surfaces forming an OCS.

The silver layer on the drilled substrate was patterned using a photolithography process to allow UV exposure to cure the UV glue while protecting the fluidic channel during the bonding step of the two substrates. For silver layer patterning, the AZ photoresist was spin-coated using a spin coater (WS-650-23, Laurel Technologies), Johnstown, PA, USA

and then baked on a hot plate at 100 °C for 1 min. The channel was then patterned under a uniform UV light using a mask aligner (OAI, Hybralign 500), Milpitas, CA, USA for 60 s at 5.7 mW/cm². The patterned drilled substrate was developed for 1 min in AZ developer, followed by a DI water rinse and N₂ drying. The exposed silver areas were etched by immersing the substrate into a silver etchant for 15 s, followed by rinse and dry steps. Then, the SOG layer was spin-coated on top of the silver layer for three purposes: 1) to protect the silver layer from possible damage during the fabrication process and testing; 2) to facilitate the silanization-based surface functionalization process for biodetection applications; and 3) maximize the sensitivity of the OCB. The SOG layer on the drilled substrate was cured at 130 °C for 4 min, followed by 120 °C for another 4 min, while the SOG layer on the plain substrate was cured at 95 °C for 1 min, followed by 200 °C for 1 min. On top of the SOG layer of the plain substrate, SU-8 2010 was spin-coated on the plain substrate at different spin speeds to achieve the optimal optical cavity width determined by simulations. Then, the SU8 was soft-baked at 95 °C for 2 min followed by UV exposure for 90 s. The postexposure bake was at 95 °C for 3 min on a hot plate. The substrate was allowed to cool for 1 min and developed in SU-8 developer for 2 min. The sample was then thoroughly rinsed with IPA, followed by N₂ dry and baked at 200 °C for 10 min.

Finally, both drilled and plain substrates were bonded together using UV glue [Fig. 1(b)]. Before the final bonding step, both substrates were incubated in 1 mL of 1% BSA for 10 min to make them more hydrophilic and thus improve the UV glue transfer. UV glue was spin-coated on a 100-mm glass “transfer” substrate. The glue on the transfer substrate was stamped onto the SU8 pattern on the plain substrate by gently pressing the plain substrate on the transfer substrate. The UV glue mostly self-applies on the SU8 pattern during this step. After the stamping step, the plain and the drilled substrate were immediately aligned and brought together using an in-house stamping/bonding stage. The sample was then cured under the mask aligner for 5 min. The typical layer thicknesses of fabricated devices are, on average, 425 nm for the SOG, 0.6–0.7 μm for the UV glue, and 9.181–9.847 μm for the SU8, depending on the spin speed. The microfluidic channel defined by the SU8 pattern has a total length of 32 mm and a width of 1 mm, and the height varies depending on the SU8 thickness.

The inlet and outlet ports were then attached to the top surface of the drilled substrate using double-sided tape (3M 468MP) for the fluid in/out of the OCS. Both inlet and outlet ports were made of acrylic and accurately machined using a laser cutter (Glowforge basic, Glowforge Inc., Seattle, WA, USA). The inlet port has an inner diameter (ID) of 2.5 mm and an outer diameter (OD) of 8 mm, while the outlet port has an ID of 1.37 mm and OD of 8 mm. A fluid was injected into the inlet port by pipetting, while a mini vacuum pump was used to flow the fluid from the inlet to the outlet through a Tygon tubing (OD 1.37 mm) attached to the outlet port. A waste container was attached between the outlet port and the vacuum pump to collect used fluid.

D. Testing Setup

A schematic and an image of the actual setup of the OCB detection system with the OCS sample location are shown in Fig. 2. Laser diode drivers powered by a 5-V power

supply were used to run the 904- and 880-nm laser diodes at 50 and 30 mA, respectively. Beams from two laser diodes were collimated, combined by a 50:50 BS, and blocked for one-second intervals by an Arduino-controlled beam blocker (BB) such that they could be imaged individually. An NF was placed in the beam's path to attenuate the intensities and avoid saturation. A mirror directed the beams toward the OCS sample and eventually a low-cost CCD camera to measure the intensities of two laser diodes.

E. RI Test

A 1.3330 RI solution was prepared by mixing DMSO with DI water. The RI of the solution was measured using a Palm Abbe digital refractometer (Misco). The initial RI solution of 1.3330 was serially diluted to obtain RI values of 1.33298, 1.33296, 1.33294, and 1.33292. The results with the 1.33292 RI fluid were used as a baseline for all measurements. Before conducting the RI tests, the microfluidic channel was thoroughly rinsed with DI water for 1–2 min and incubated for 1 h for stabilization. To perform the measurements, 7 μL of each RI solution (ranging from 1.33292 to 1.33300) was introduced starting from the lowest RI fluid. Each solution was injected into the inlet port of the channel at a flow rate of 8.2 $\mu\text{L}/\text{min}$, with a 40-s interval between successive injections. To prevent the channel from being completely emptied at any point, a residual volume of 1.5 μL of the solution was consistently retained within the inlet port and the channel before the introduction of each subsequent solution. This method ensured that the resultant RI values were closely aligned with the initially introduced RI values. Following the series of RI solution measurements, the channel was thoroughly rinsed with DI water (200 μL) and the signal returned back to the initial baseline level.

The optical intensity was captured by the CCD camera in real time with a shutter time of either 1 or 1.5 ms. All measurements were conducted on three different fabricated OCS, and the mean value of the replicates, along with the standard deviations and standard errors from the mean, were used to report the results. This ensured robustness and reliability, showcasing the repeatability of the tests.

F. Data Collection and Processing

The data acquisition process involved collecting signals from a data processing region (DPR), a circular region in the middle of the channel with a diameter of 188 μm (50 pixels). This DPR was positioned where two laser diode intensities change in opposite directions. The average intensities of the DPR were calculated for each laser diode from the collected CCD images. The CCD image data acquisition and differential value calculation were performed by IgorPro while the data were analyzed and displayed via OriginPro.

III. RESULTS AND DISCUSSION

A. Simulation Results

Fig. 3(a)–(d) shows the simulated transmission efficiency of each silver thickness for an optical cavity width range of 120 nm that includes the optimal optical cavity width. As described earlier, based on the measurements, silver thicknesses of 22.5, 46.9, 58.3, and 76.2 nm were used for simulations. As the silver thickness increases, the transmission curve

becomes sharper while the peak efficiency decreases. This is due to two properties of the silver layer increasing: reflectance, which enhances the optical resonance, and absorption, which increases the loss, thus reducing overall efficiency. The optical cavity width where the efficiencies of the two wavelengths change linearly is determined to be the optimal cavity width for a silver thickness because, at that optical cavity width, a small bulk or local RI change (equivalent effect of a slight increase in the optical cavity width) within the OCS will induce the largest possible change in the transmitted optical intensity. Based on the simulation results, the optimal cavity widths were determined to be 10.539, 9.881, 10.218, and 10.547 μm for the silver thicknesses of 22.5, 46.9, 58.3, and 76.2 nm, respectively.

To calculate the differential values, we first used the following differential equation:

$$\eta = \frac{I_1 - I_{10}}{I_{10}} - \frac{I_2 - I_{20}}{I_{20}}. \quad (1)$$

In this equation, I_1 (increasing) and I_2 (decreasing) represent the intensities (or efficiencies for simulations) of λ_1 and λ_2 , respectively, while I_{10} and I_{20} represent the initial intensities for I_1 and I_2 , respectively. The calculated differential values produced by a bulk RI change compared to the baseline RI of 1.33292 for those four different silver thicknesses with the optimal cavity widths are shown in Fig. 3(e). The differential value slopes for the RI range are then calculated. The higher the slope, the greater is the sensitivity. The slopes for the silver thicknesses of 22.5, 46.9, 58.3, and 76.2 nm were 1692.5, 6402.0, 8646.3, and 10134.5, respectively. As expected, the slope is larger for a thicker silver thickness due to a stronger optical resonance. However, the slope for the silver thickness of 76.2 nm is only slightly higher than that of 58.3 nm due to the increased absorption loss.

B. Measurement Results

To experimentally determine the optimal silver thickness and corresponding optical cavity width, we fabricated OCSs with four different silver thicknesses and performed the bulk RI measurements. We used the fabrication processes described earlier in Section II-C for all OCSs. Only the silver deposition times and SU8 spin speeds varied between different OCSs. For each silver thickness, we initially fabricated an OCS with the optical cavity width determined from the simulation. Then, the actual optimal optical cavity width and corresponding SU8 spin speed were determined based on the measurements. To determine the optimal optical cavity width experimentally, we fabricated several different OCSs with different SU8 spin speeds for each silver thickness and injected the DI water into the channel. When the channel was filled, the intensities of the two wavelengths changed over time due to the swelling of the SU8 and UV glue, thus effectively changing the cavity size. At the optimal optical cavity width, those two wavelengths must change in opposite directions linearly.

The microfluidic channel design with respect to a 3" glass substrate is shown in Fig. 4(a), while Fig. 4(b) shows the typical CCD images of two wavelengths with lines to visualize the microfluidic channel and the circular DPR. When the intensities began changing linearly in

opposite directions, we introduced the baseline fluid with a 1.33292 RI followed by 1.33294, 1.33296, 1.33298, and 1.3330. At the end of the measurements, the microfluidic channel was rinsed thoroughly using DI water as described earlier in Section II-E. Fig. 4(c) shows the intensity measurement results for the OCS with a silver thickness of 46.9 nm as an example. The differential values are calculated using (1) and shown in Fig. 4(d).

Fig. 5(a) shows the triplicate RI measurement results for four different silver thicknesses with corresponding optimal optical cavity widths. The optimal optical cavity widths determined experimentally were 10.6, 9.9, 10.2, and 10.5 μm for the silver thicknesses of 22.5, 46.87, 58.33, and 76.23 nm, respectively (considering the UV-glue thickness of 0.7 μm). This result matches very well with the simulation results. The slopes of the line fits of the measured data were 878.2, 1956.4, 2995.9, and 2154.2 for the silver thicknesses of 22.5, 46.87, 58.33, and 76.23 nm, respectively. The R -squared values for the line fits were 0.97 (22.5 nm), 0.99 (46.87 nm), 0.95 (58.3 nm), and 0.98 (76.23 nm). Compared to simulations, the overall slopes were less and the slope for the 76.23-nm silver thickness was less than that of 58.33 nm. This could be due to higher absorption loss of the sputter-deposited silver layer than that used in the simulation and other additional losses. Recognizing these factors, we strategically selected a silver thickness range of 22.5–76.23 nm to find an optimal balance between reflectivity and absorption properties. It is noteworthy that, although the 58.33-nm silver thickness demonstrated the largest slope, it also exhibited larger error bars (\pm one standard deviation of three samples) indicating significant sample-to-sample variation compared to the 22.5- and 46.87-nm silver thicknesses.

The larger error bars observed for the 58.3- and 76.23-nm silver thickness samples can be attributed to variations in the SU-8 layer thickness during the fabrication of the OCS. We noted a sample-to-sample fabrication tolerance of approximately ± 50 nm. This discrepancy in the SU-8 layer thickness can induce noticeable variations in the optical properties of the cavities. The implications of these variations are particularly pronounced in high Q -factor cavities, such as those fabricated with thicker silver layers, which exhibit heightened sensitivity to even minor inconsistencies. Consequently, this sensitivity is reflected in the larger error bars observed in our results, where the high Q -factor amplifies the effects of these small variations, leading to a larger discrepancy in the measured intensities.

The LOD for each silver thickness was determined by $(3.3 \times \sigma)/\text{slope}$, where σ is the standard deviation of the blank signal (RI 1.33292). The calculated LOD is shown in Fig. 5(b). Among all silver thicknesses, the OCS with 46.9 nm (22.5-s silver deposition time) of silver produced the lowest LOD of 3.37×10^{-6} refractive index unit (RIU). Even though the slope of the 58.3-nm silver was larger than any other silver thickness, its larger blank signal standard deviation (i.e., higher noise) due to its high Q -factor makes the LOD worse than thinner silver layer OCSs. Based on the measurement results, we concluded that the silver thickness of 46.87 nm is the best out of those four different silver thicknesses we compared.

C. Improving the LOD of the OCB

To improve the LOD of the OCB further, we investigated a longer camera shutter time and a different differential equation. The camera shutter time, also known as the exposure time, refers to the duration for which the camera's shutter remains open, allowing light to reach

the camera sensor. The results shown in Figs. 4 and 5 used a 1-ms shutter time. The larger the camera shutter time, the larger the overall measured intensities, which could improve the LOD of the OCB. To investigate the impact of a longer shutter time, we conducted RI measurements for a 46.87-nm sample again with a 1.5-ms shutter time which was the highest we could use without saturating the CCD camera. As shown in Fig. 6(a), increasing the camera shutter time resulted in brighter images due to the longer exposure to light. With a 1.5-ms shutter time, the LOD improved by a factor of 1.26 (from 3.37×10^{-6} to 2.68×10^{-6} RIU) compared to the 1-ms shutter time [Fig. 6(b)].

Detailed data analyses led to the conclusion that the differential equation shown in (1) primarily relies on the ratio change of the wavelength whose intensity goes up as the RI inside the OCS increases. This is because the initial intensity of the wavelength whose intensity goes down as the RI increases is always the largest compared to the measured intensities for the higher RI. To mitigate this issue, we introduced a new differential equation

$$\eta = \frac{I_1 - I_{10}}{I_{10}} - \frac{I_2 - I_{20}}{I_2} \quad (2)$$

where I_{10} and I_{20} denote the initial intensities for the RI of 1.33292 for λ_1 (increasing) and λ_2 (decreasing), respectively, and I_1 and I_2 are the measured intensities for other higher RIs as before. The only difference between (1) and (2) is the denominator of the second part of the equation. By replacing I_{20} with I_2 , (2) enhances the ratio change of λ_2 . The measured data with a 1.5-ms shutter time shown in Fig. 6 were processed again with (2) to determine the LOD. As shown in Fig. 7(a), the slope has increased as expected. Fig. 7(b) shows the LOD with the new differential equation compared to the old one. With (2), the LOD improved by a factor of 1.09 (from 2.68×10^{-6} to 2.47×10^{-6} RIU) compared to that calculated with (1).

Finally, the LOD of the OCB based on the RI measurements was determined to be 2.47×10^{-6} RIU after the optimization of the silver layer thickness, shutter time, and differential equation. Table I shows the comparison of this LOD compared to other approaches reported in the literature. The OCB developed in this work exhibits a high sensitivity compared to other referenced biosensors. Even though there could be different applications for different biosensor types, the OCB with the improved LOD clearly indicates its potential for detecting small changes in bulk and local RI within the OCS.

IV. CONCLUSION

In this article, we optimized the OCS and investigated detection and data processing methods to improve the LOD. Based on the simulations, we optimized our fabrication process for each silver thickness we tried. The LOD for bulk RI fluid in the range of 1.33292–1.333 for each silver thickness was determined and compared. The triplicate RI measurement results showed that the optimal silver thickness is 46.87 nm. Additionally, we investigated the impact of camera shutter time on device performance and a new differential equation. Extending the shutter time to 1.5 ms resulted in increased differential values and an improved LOD by a factor of 1.26 compared to the 1-ms shutter time. By modifying the

equation to consider the ratio changes of both laser diodes, the LOD was improved further to 2.47×10^{-6} RIU, which is better than other recently reported biosensors. Considering its demonstrated high sensitivity, easy fabrication process, and low-cost detection components without requiring labeling or complex alignment procedures, we demonstrated the OCB is an attractive POCT biosensor option.

Acknowledgments

This work was supported by the National Institute of General Medical Sciences (NIGMS) of the National Institutes of Health under Award R15GM146233. The associate editor coordinating the review of this article and approving it for publication was Dr. Daniele Tosi.

Biographies



Marzhan Sypabekova received the B.S. degree in biotechnology from the University of Glasgow, Glasgow, U.K., in 2011, the M.S. degree in bionanophotonics for telecommunications and biology from Ecole Normale Supérieure de Cachan, Cachan, France, in 2014, and the Ph.D. degree in science engineering and technology from Nazarbayev University, Astana, Kazakhstan, in 2019.

From 2019 to 2021, she was a Postdoctoral Researcher with the Biosensors and Bioinstruments Laboratory, Astana. Since 2021, she has been a Postdoctoral Research Associate with the Electrical and Computer Engineering Department, Baylor University, Waco, TX, USA. Her research interests include the development of point-of-care devices, biosensors (electrochemical, optical, and fiber optic), and biosensor surface chemistry optimization.

Dr. Sypabekova was a recipient of the Newton-AI Farabi Researchers Links Award (British Council) and IEEE Sensors Travel Award. She is a member of the Biomedical Engineering Society.



Aidan Hagemann received the B.S. degree in biomedical engineering from LeTourneau University, Longview, TX, USA, in 2020. He is currently pursuing the Ph.D. degree in electrical engineering with Baylor University, Waco, TX.

He has authored one review article regarding the 3-Aminopropyl Triethoxysilane (APTES) functionalization process. His research interests are point-of-care biosensors, optical biosensors, and microfabrication.



Jenna Kleiss is currently pursuing the B.S. degree in general engineering with Baylor University, Waco, TX, USA, with a biomedical concentration.

She is currently an Undergraduate Researcher with the Bio and Micro Devices Laboratory and an Engineering Ambassador of the Engineering and Computer Science Department, Baylor University.

Ms. Kleiss is a member of the Society of Women Engineers.



Cooper Morlan is pursuing the B.S. and subsequently M.S. degrees in electrical and computer engineering with Baylor University, Waco, TX, USA.

In 2021, he joined Community Psychiatry, Sacramento, CA, USA, as a Customer Service/Data Entry Clerk. Since 2022, he has been an Undergraduate Researcher with the Bio and Micro Devices Laboratory, Baylor University. His research interests include optical cavity resonator applications, antigen–antibody bindings, and lasing medium applications.

Mr. Morlan is a member of Computing for Compassion and the National Society of Collegiate Scholars.



Seunghyun Kim (Member, IEEE) received the Ph.D. degree in optical science and engineering from the University of Alabama in Huntsville, Huntsville, AL, USA, in 2004.

He was a Research Associate with Brigham Young University, Provo, UT, USA, from 2005 to 2010. He joined LeTourneau University, Longview, TX, USA, as an Assistant Professor, in 2010, where he was promoted to Associate Professor in 2015. In 2016, he moved to Baylor University, Waco, TX. His extensive research work in bio/chemical sensors,

integrated optics, photonic crystals, and micro- and nanofabrication became four patents, 38 refereed journal articles, and 60 conference abstracts and proceedings.

Dr. Kim is a Senior Member of Optica and a member of the Biomedical Engineering Society. He received the NSF CAREER Award in 2014 and was selected for the Outstanding Professor Award for distinctive scholarship at Baylor University in 2018.

REFERENCES

- [1]. Kim J, Campbell AS, de Ávila BE-F, and Wang J, “Wearable biosensors for healthcare monitoring,” *Nature Biotechnol*, vol. 37, no. 4, pp. 389–406, Apr. 2019, doi: 10.1038/s41587-019-0045-y. [PubMed: 30804534]
- [2]. Liu D et al. , “Trends in miniaturized biosensors for point-of-care testing,” *TrAC Trends Anal. Chem*, vol. 122, Jan. 2020, Art. no. 115701, doi: 10.1016/j.trac.2019.115701.
- [3]. Wang X, Li F, and Guo Y, “Recent trends in nanomaterial-based biosensors for point-of-care testing,” *Frontiers Chem.*, vol. 8, Oct. 2020, Art. no. 586702. [Online]. Available: 10.3389/fchem.2020.586702
- [4]. Choi JR, “Development of point-of-care biosensors for COVID-19,” *Frontiers in Chemistry*, vol. 8, p. 517, May 2020, doi: 10.3389/fchem.2020.00517. [PubMed: 32574316]
- [5]. Land KJ, Boeras DI, Chen X-S, Ramsay AR, and Peeling RW, “REASSURED diagnostics to inform disease control strategies, strengthen health systems and improve patient outcomes,” *Nature Microbiology*, vol. 4, no. 1, pp. 46–54, Dec. 2018, doi: 10.1038/s41564-018-0295-3.
- [6]. Noah NM and Ndangili PM, “Current trends of nanobiosensors for point-of-care diagnostics,” *J. Anal. Methods Chem*, vol. 2019, Oct. 2019, Art. no. 2179718, doi: 10.1155/2019/2179718.
- [7]. Salek-Maghsoudi A et al. , “Recent advances in biosensor technology in assessment of early diabetes biomarkers,” *Biosensors Bioelectron*, vol. 99, pp. 122–135, Jan. 2018, doi: 10.1016/j.bios.2017.07.047.
- [8]. Andryukov BG, Besednova NN, Romashko RV, Zaporozhets TS, and Efimov TA, “Label-free biosensors for laboratory-based diagnostics of infections: Current achievements and new trends,” *Biosensors*, vol. 10, no. 2, p. 11, Feb. 2020, doi: 10.3390/bios10020011. [PubMed: 32059538]
- [9]. Inan H et al. , “Photonic crystals: Emerging biosensors and their promise for point-of-care applications,” *Chem. Soc. Rev*, vol. 46, no. 2, pp. 366–388, 2017, doi: 10.1039/C6CS00206D. [PubMed: 27841420]
- [10]. Sin ML, Mach KE, Wong PK, and Liao JC, “Advances and challenges in biosensor-based diagnosis of infectious diseases,” *Exp. Rev. Mol. Diagnostics*, vol. 14, no. 2, pp. 225–244, Mar. 2014, doi: 10.1586/14737159.2014.888313.
- [11]. Neilson KA et al. , “Less label, more free: Approaches in label-free quantitative mass spectrometry,” *PROTEOMICS*, vol. 11, no. 4, pp. 535–553, Feb. 2011, doi: 10.1002/pmic.201000553. [PubMed: 21243637]
- [12]. Sanko V and Kuralay F, “Label-free electrochemical biosensor platforms for cancer diagnosis: Recent achievements and challenges,” *Biosensors*, vol. 13, no. 3, p. 333, Mar. 2023. [Online]. Available: <https://www.mdpi.com/2079-6374/13/3/333> [PubMed: 36979545]
- [13]. Khansili N, Rattu G, and Krishna PM, “Label-free optical biosensors for food and biological sensor applications,” *Sens. Actuators B, Chem*, vol. 265, pp. 35–49, Jul. 2018, doi: 10.1016/j.snb.2018.03.004.
- [14]. Pirzada M and Altintas Z, “Recent progress in optical sensors for biomedical diagnostics,” *Micromachines*, vol. 11, no. 4, p. 356, Mar. 2020, doi: 10.3390/mi11040356. [PubMed: 32235546]
- [15]. Gauglitz G, “Critical assessment of relevant methods in the field of biosensors with direct optical detection based on fibers and waveguides using plasmonic, resonance, and interference effects,” *Anal. Bioanal. Chem*, vol. 412, no. 14, pp. 3317–3349, May 2020, doi: 10.1007/s00216-020-02581-0. [PubMed: 32313998]

- [16]. Pathak AK, Singh VK, Ghosh S, and Rahman BMA, "Investigation of a SPR based refractive index sensor using a single mode fiber with a large D shaped microfluidic channel," *OSA Continuum*, vol. 2, pp. 3008–3018, Nov. 2019, doi: 10.1364/OSAC.2.003008.
- [17]. Tobore TO, "On the need for the development of a cancer early detection, diagnostic, prognosis, and treatment response system," *Future Sci. OA*, vol. 6, no. 2, Nov. 2019, Art. no. Fso439, doi: 10.2144/fsoa-2019-0028.
- [18]. Cho S, Brake J, Joy C, and Kim S, "Refractive index measurement using an optical cavity based biosensor with a differential detection," *Proc. SPIE*, vol. 9332, Mar. 2015, Art. no. 2079300.
- [19]. Rho D and Kim S, "Demonstration of a label-free and low-cost optical cavity-based biosensor using streptavidin and C-reactive protein," *Biosensors*, vol. 11, no. 1, p. 4, 2021. [Online]. Available: <https://www.mdpi.com/2079-6374/11/1/4>
- [20]. Rho D, Breaux C, and Kim S, "Demonstration of a low-cost and portable optical cavity-based sensor through refractive index measurements," *Sensors*, vol. 19, no. 9, p. 2193, May 2019, doi: 10.3390/s19092193. [PubMed: 31083614]
- [21]. Cowles P, Joy C, Bujana A, Rho D, and Kim S, "Preliminary measurement results of biotinylated BSA detection of a low cost optical cavity based biosensor using differential detection," *Proc. SPIE*, vol. 9725, Apr. 2016, Art. no. 972509.
- [22]. Joy C and Kim S, "Benefits of a scaled differential calculation method for use in a Fabry–Pérot based optical cavity biosensor," in *Proc. Texas Symp. Wireless Microw. Circuits Syst. (WMCS)*, Mar. 2017, pp. 1–4, doi: 10.1109/WMCaS.2017.8070707.
- [23]. Rho D and Kim S, "Low-cost optical cavity based sensor with a large dynamic range," *Opt. Exp.*, vol. 25, no. 10, pp. 11244–11253, May 2017, doi: 10.1364/OE.25.011244.
- [24]. Rho D and Kim S, "Label-free real-time detection of biotinylated bovine serum albumin using a low-cost optical cavity-based biosensor," *Opt. Exp.*, vol. 26, no. 15, pp. 18982–18989, Jul. 2018, doi: 10.1364/OE.26.018982.
- [25]. Bahadoran M, Seyfari AK, Sanati P, and Chua LS, "Label free identification of the different status of anemia disease using optimized double-slot cascaded microring resonator," *Sci. Rep.*, vol. 12, no. 1, p. 5548, Apr. 2022, doi: 10.1038/s41598-022-09504-2. [PubMed: 35365740]
- [26]. Kisku S, Sarwagya K, and Ranjan S, "Performance investigation of triple unsymmetrical microring resonator as optical filter as well as biosensor," *Opt. Quantum Electron.*, vol. 55, no. 2, p. 164, Feb. 2023, doi: 10.1007/s11082-022-04443-8. [PubMed: 36618533]
- [27]. Shi B, Chen X, Cai Y, Zhang S, Wang T, and Wang Y, "Compact slot microring resonator for sensitive and label-free optical sensing," *Sensors*, vol. 22, no. 17, p. 6467, Aug. 2022. [Online]. Available: <https://www.mdpi.com/1424-8220/22/17/6467> [PubMed: 36080926]
- [28]. Kolli VR, Basavaprasad, and Talabattula S, "High Q photonic crystal based microring resonator biosensor for the detection of glucose-concentration in urine and blood," in *Proc. IEEE Int. Conf. Electron., Comput. Commun. Technol. (CONECCT)*, Jul. 2020, pp. 1–4, doi: 10.1109/CONECCT50063.2020.9198624.
- [29]. Liu L, Hu Z, Ye M, Yu Z, Ma C, and Li J, "On-chip refractive index sensor with ultra-high sensitivity based on sub-wavelength grating racetrack microring resonators and Vernier effect," *IEEE Photon. J.*, vol. 14, no. 5, pp. 1–7, Oct. 2022, doi: 10.1109/JPHOT.2022.3199908.
- [30]. Tang T, Wu X, Liu L, and Xu L, "Packaged optofluidic microbubble resonators for optical sensing," *Appl. Opt.*, vol. 55, no. 2, pp. 395–399, Jan. 2016. [PubMed: 26835777]
- [31]. Merabet NA, Cherbi L, Haddouche I, Benlacheheb M, and Yu J, "Glycosuria monitoring based on whispering gallery mode resonator biosensor," *J. Opt.*, vol. 52, no. 3, pp. 1047–1055, Sep. 2023, doi: 10.1007/s12596-022-00933-w.
- [32]. Tang S et al. , "Fabry–Pérot interferometer based on a fiber-tip fixed-supported bridge for fast glucose concentration measurement," *Biosensors*, vol. 12, no. 6, p. 391, Jun. 2022. [Online]. Available: <https://www.mdpi.com/2079-6374/12/6/391> [PubMed: 35735540]
- [33]. Wang R et al. , "Label-free and selective cholesterol detection based on multilayer functional structure coated fiber Fabry–Pérot interferometer probe," *Analytica Chim. Acta*, vol. 1252, Apr. 2023, Art. no. 341051, doi: 10.1016/j.aca.2023.341051.
- [34]. Sypabekova M, Amantayeva A, Gonzalez-Vila A, Shaimerdenova M, Caucheteur C, and Tosi D, "Spectral characteristics and interrogation of a fiber-optic ball resonator biosensor modulated

by a tilted fiber Bragg grating,” *Opt. Fiber Technol*, vol. 79, Sep. 2023, Art. no. 103354, doi: 10.1016/j.yofte.2023.103354.

Author Manuscript

Author Manuscript

Author Manuscript

Author Manuscript

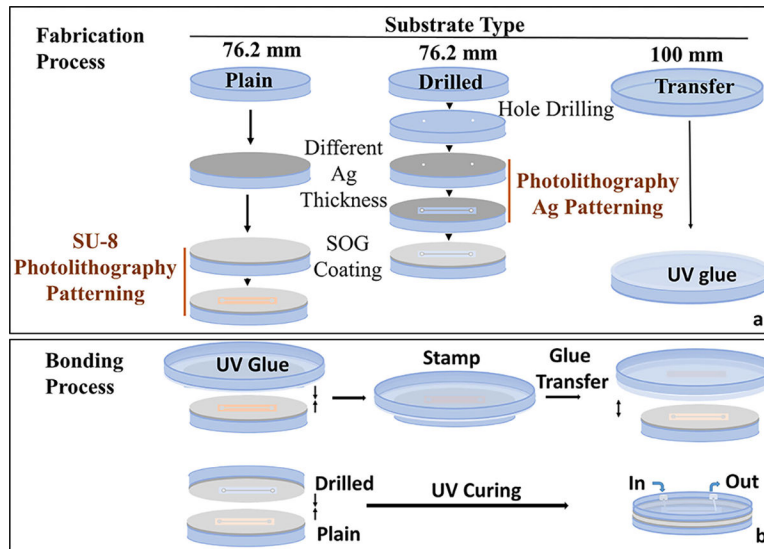


Fig. 1. OCS fabrication process: (a) substrate preparation and fabrication step and (b) bonding step.

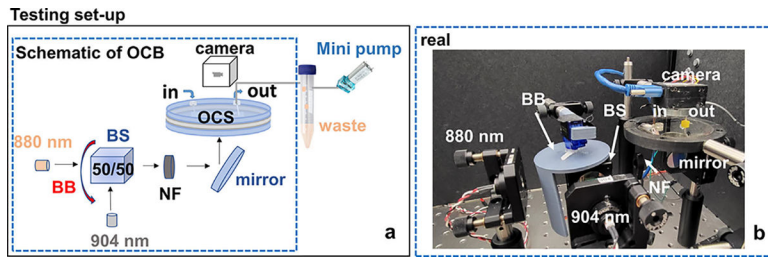


Fig. 2.

(a) Schematic of the testing setup for the OCB. The blue dashed line represents components positioned inside the dark box to block ambient light. (b) Real image of the blue dashed line part of the schematic.

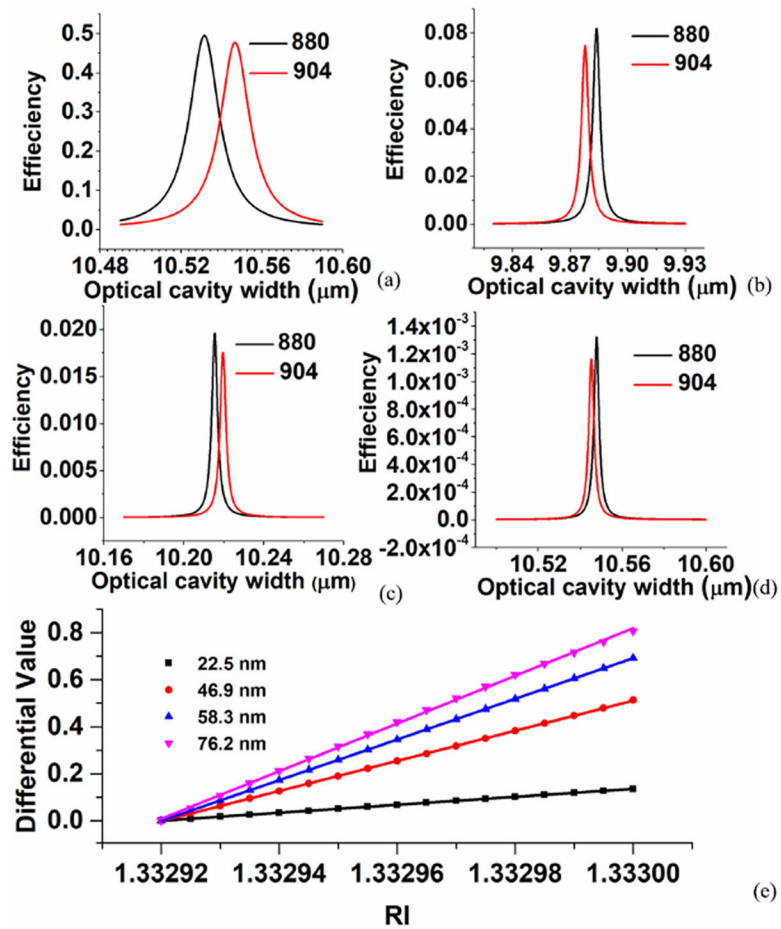


Fig. 3. Simulations for silver thicknesses of: (a) 22.6 nm; (b) 46.9 nm; (c) 58.3 nm; and (d) 76.2 nm. (e) Simulation of the differential value produced by a bulk RI change with an initial RI of 1.3329 at silver thicknesses of 22.6, 46.9, 58.3, and 76.2 nm.

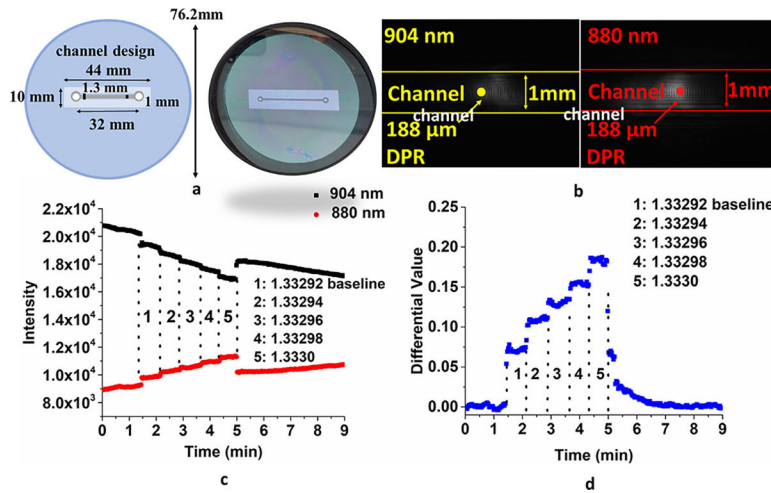


Fig. 4. (a) Microfluidic channel design with dimensions and real image of the OCS. (b) Example resonance beam profile images for laser diodes at 904 and 880 nm. (c) Example RI measurement results. (d) Calculated differential values for the data in (c) using (1).

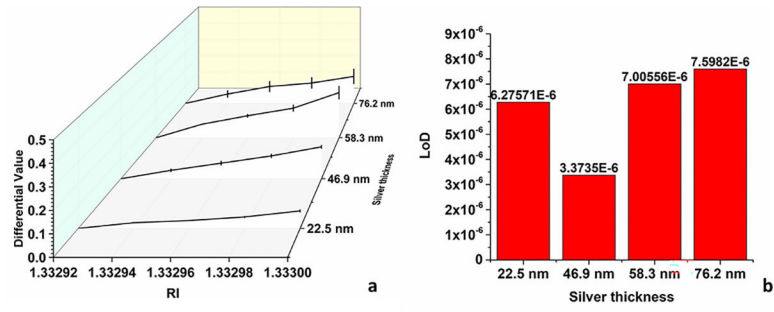


Fig. 5. (a) Differential values versus RI from 1.33292 to 1.333 and (b) LOD for four silver thicknesses.

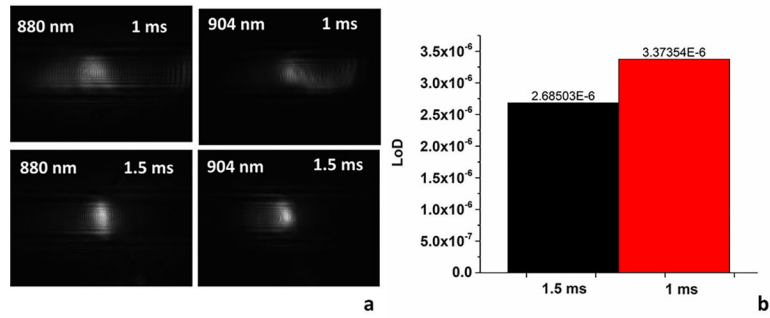


Fig. 6. (a) Example CCD images showing the beam profile at shutter times 1 and 1.5 ms. (b) Comparison of LOD for camera shutter times 1 and 1.5 ms.

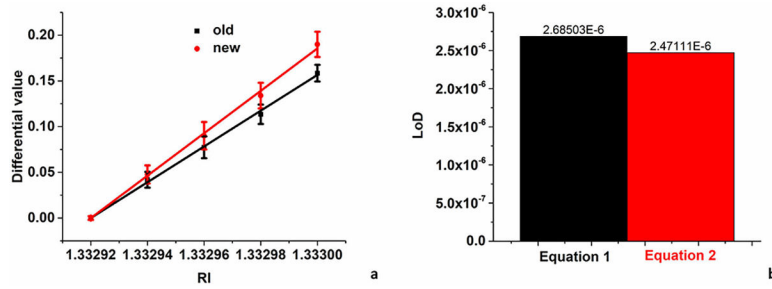


Fig. 7. (a) Differential values (shutter time: 1.5 ms) versus RI using old and new differential equations. Linear fitting was used to determine the LOD. (b) Comparison of LOD between old and new differential equations.

Author Manuscript

Author Manuscript

Author Manuscript

Author Manuscript

TABLE I

Comparison of LOD for Optical Biosensors Published in 2022–2023. The Value for LOD for Some Examples Was Calculated in RIU Based on the Data Given in Respective Published Work

Biosensor type	LOD (RIU)	ref
1 Optical Cavity	2.47×10^{-6}	This work
	1.73×10^{-5}	[20]
2	4.88×10^{-6}	[25]
3	7.00×10^{-6}	[26]
4 Micro-ring resonator	2.32×10^{-4}	[27]
	5.1282	[28]
	1.74×10^{-5}	[29]
7 Whispering gallery mode	5.4×10^{-5}	[30]
	1×10^{-4}	[31]
9 Fabry Perot interferometer	2.4×10^{-4}	[32]
	14.2×10^{-3}	[33]
11 Optical fiber ball resonator	6.47×10^{-3}	[34]